Journal of Petroleum Science and Engineering 189 (2020) 107010

Contents lists available at ScienceDirect

Journal of Petroleum Science and Engineering

journal homepage: http://www.elsevier.com/locate/petrol

Using pressure pulse decay experiments and a novel multi-physics shale transport model to study the role of Klinkenberg effect and effective stress on the apparent permeability of shales

Zihao Li, Nino Ripepi, Cheng Chen *

Virginia Tech, USA

ARTICLE INFO

Keywords:
Apparent permeability
Klinkenberg effect
Shale gas
Biot's coefficient
Multi-physics shale transport

ABSTRACT

The confining pressure imposed on a shale formation has a significant impact on the apparent permeability of the rock. Gas flow in low-permeability shales differs significantly from liquid flow because of the Klinkenberg effect, which results from gas molecule slip at the wall surfaces inside the nanopores. This effect causes the increase of apparent permeability (i.e., the measured permeability). In this study, cores extracted from four U.S. shale formations were tested using a pulse decay permeameter (PDP) under varying combinations of confining and pore pressures. The Klinkenberg coefficient was calculated to interpret the change in the measured apparent permeability as a function of pore pressure and effective stress. Next, based on the various combinations of confining and pore pressures, the actual values of the Biot coefficient were calculated by data fitting. Moreover, the samples were cored in the directions parallel to and perpendicular to the shale bedding planes to unravel the role of bedding plane direction on the apparent permeability. Furthermore, a novel, multi-physics shale transport (MPST) model was developed to account for the coupled multi-physics processes of geomechanics, fluid dynamics, and Klinkenberg effect for gas transport in shales. In the MPST model, pore pressure and effective stress are the two independent input variables, and the measured apparent permeability is the model output. The MPST model was then used to fit the PDP experimental data, and the successful data fitting confirmed that the MPST model captures the critical multi-physics processes that regulate the apparent permeability.

1. Introduction

The complicated petrophysical properties and extremely low permeability of shale formations lead to tremendous challenges to develop the hydrocarbon resources trapped in these formations. Horizontal drilling associated with multi-stage hydraulic fracturing has become an effective technique to produce hydrocarbon resources from shales at an economically viable rate (Economides and Nolte, 2000; Gu and Mohanty, 2014; Chen et al., 2015a, 2016; Hu et al., 2018). During hydrocarbon recovery, the decreased pore pressure leads to increased effective stress and fracture closure (Fan et al., 2017b, 2018). The effective stress variation has a significant impact on the petrophysical properties in the shale formation, especially the formation permeability. It is thus crucial to investigate the relationship between formation permeability and effective stress variation.

The investigation of the correlation between effective stress and rock permeability started from laboratory analysis of tight sandstones. Warpinski and Teufel (1992) performed laboratory experiments to study the Biot's coefficient in tight sandstone and chalk. They found that the Biot's coefficient in tight sandstone was close to unity for small effective stresses but contained uncertainties for larger effective stresses. The value of Biot's coefficient varied with both effective stress and pore pressure. Ojala and Fjær (2007) tested Castlegate sandstone cores under cyclic pore and confining pressure variations. Their results demonstrated that the Biot's coefficient in sandstone under acoustic and elastic testing can be considerably different from unity. They also illustrated the hysteresis in petrophysical properties due to microfractures or frictional effects. The research on shale rock permeability and effective stress has also been conducted extensively. Chen et al. (2015b) derived a theoretical model between shale permeability and effective stress. They also investigated the correlation between fracture compressibility, shale properties, and reservoir pressure. Cui et al., (2018) discussed Chen's model and utilized strain evolution to investigate how shale permeability changes with time and gas pressure in the matrix system, which

* Corresponding author.
E-mail address: chen08@vt.edu (C. Chen).

https://doi.org/10.1016/j.petrol.2020.107010
Received 7 June 2019; Received in revised form 1 December 2019; Accepted 28 January 2020
Available online 31 January 2020

confirms that it is important to include the interactions between shale microstructures and gas transport processes. Although the Biot's coefficient is a widely used poroelastic parameter in calculating the effective stress, its value is usually assumed to be one for the sake of simplicity in many applications when no other information is available. (e.g., Alam et al., 2014; Bhandari et al., 2015; Jin et al., 2015; Rydzy et al., 2016).

The Klinkenberg effect was a theory developed by Klinkenberg (1941) to explain the abnormal phenomenon of apparent permeability enhancement for gas flow in nanopores. It has a significant impact on gas flow in low-permeability porous media such as shale reservoirs and tight coalbeds (Wu and Pruess, 1998). The Klinkenberg effect is related to the Knudson number (Kn), which is defined as $Kn = \lambda/d$, where λ is the gas mean-free-path length (m) and d is pore diameter (m). When $Kn < 0.001$, gas flow is governed by the Navier-Stokes equations with a no-slip boundary condition on the pore walls. When $0.001 < Kn < 0.1$, gas flow is in the slip flow regime in which the non-continuum effect can be approximated by a velocity slip on the pore walls; the bulk gas flow can still be governed by the Navier-Stokes equation (Beskok and Karniadakis, 1999). The continuous increase in Kn leads to the transitional flow regime ($0.1 < Kn < 10$) and then the free molecular flow regime ($Kn > 10$), where the gas flow cannot be described by the Navier-Stokes equations (Tian et al., 2019).

In a shale formation, when the nanopore diameter decreases or gas pressure decreases, the Kn number increases because a lower gas pressure leads to a larger gas molecule mean-free-path length. In this case, the nanopore diameter is comparable to or smaller than the mean-free-path length of gas molecules. As a consequence, gas molecules collide with the pore walls more frequently than with one another, leading to Knudsen diffusion that causes a slip-velocity boundary condition in the macroscopic Navier-Stokes flow model (Javadpour, 2009). The existence of the slip velocity on flow boundaries enhances the overall mass flux through the nanopore, which results in increased apparent permeability of the shale (Chen, 2016).

A series of analytical solutions was developed to characterize gas flow in tight porous media subjected to the Klinkenberg effect (Wu and Pruess, 1998; Innocentini and Pandolfelli., 2001; Zhu et al., 2007; Hu et al., 2009; Hayek, 2015). Li et al. (2016) derived an analytical formula for gas effective permeability subjected to the Klinkenberg effect based on the microscale flow model and fractal capillary model. Their results demonstrated the physical meaning of the model parameters. In a complex environment, such as polymer-water-oil flow in porous media, the Klinkenberg effect was found to be mitigated with the presence of an adsorption polymer layer (Blanchard et al., 2007). Moreover, the Klinkenberg coefficient cannot be treated as a constant in coalbeds due to the high compressibility and matrix swelling of coal (Wang et al., 2014). All the studies reviewed above confirm that the Klinkenberg effect exists in a wide range of subsurface flow and transport processes associated with numerous geoenergy and geoenvironmental applications.

In this paper, core samples were collected from four U.S. shale formations, including the Mancos, Eagle Ford, Barnett, and Marcellus shales, to investigate the correlations between apparent permeability, pore pressure, and confining pressure. By testing cores having varying bedding plane directions, the role of bedding plane direction on the apparent permeability was unraveled. In this work, a core sample's apparent permeability was tested using a pressure pulse decay permeameter (PDP) under various combinations of pore pressure and confining pressure. The Klinkenberg coefficient was calculated to explain the change of the measured apparent permeability as a function of pore pressure and effective stress. A multi-physics shale transport (MPST) model was developed, which accounts for the coupled multi-physics processes of fluid dynamics, geomechanics, and the Klinkenberg effect for gas transport in shales. The fitting curves were then compared with experimental data. The comprehensive experimental and model fitting aim to advance the fundamental understanding of the role of confining pressure, pore pressure, Klinkenberg effect, and bedding plane direction on the apparent permeability. The MPST model development aims to answer the question if it is possible to predict and fit laboratory data for the measured apparent permeability of a shale using pore pressure and effective stress change as model inputs. The research outcome has the potential to advance the scientific understanding of the relationship between geomechanical stresses and gas flow properties in a shale formation.

2. Overview of the experimental and modeling workflow

This section provides an overview of the entire experimental and modeling workflow. Details of experimental setup will be given in a later section. In this work, an experiment and modeling approach was developed to study the correlation between apparent permeability, confining pressure, and pore pressure. First, a series of shale core samples, having different bedding plane directions, was extracted from four U.S. shale formations. Second, a laboratory PDP was used to measure the apparent permeabilities under a wide range of different combinations of pore pressure and confining pressure. Third, we derived the Klinkenberg coefficient to explain the change of the measured apparent permeability as a function of pore pressure and effective stress; in this process the Biot's coefficient is assumed to be one for the sake of simplicity. Fourth, the actual values of the Biot's coefficient were calculated by data fitting based on the laboratory measurements obtained under various combinations of pore and confining pressures. Finally, a MPST model was developed to account for the coupled multi-physics processes of fluid dynamics, geomechanics, and the Klinkenberg effect for gas transport in shales, and to predict the dependence of a shale's apparent permeability on pore pressure and effective stress. The laboratory PDP data were then fitted to the MPST model. Fig. 1 illustrates an overview of the experiment and modeling workflow.

In this study, based on the hardware limit of the PDP equipment, eight pore pressure values (100 psi, 300 psi, 500 psi, 700 psi, 900 psi, 1100 psi, 1300 psi, and 1500 psi) were used in the PDP testing. For each pore pressure value, three confining pressure values were applied, which were 500 psi, 1000 psi, and 1500 psi higher than the pore pressure, separately. Therefore, for a single shale core, 24 apparent permeability measurements in total were conducted using the PDP based on the different combinations between pore pressure and confining pressure. The experimental results of the cores that were from the same formation but had different bedding plane directions were compared to improve the understanding of the role of bedding plane direction on the measured apparent permeability. Fig. 2 demonstrates an overview of the shale core samples tested in this work using the PDP equipment, which were collected from four different U.S. shale formations including the Eagle Ford, Marcellus, Mancos, and Barnett formations, with the TOCs measured as 2.02%, 4.45%, 1.37%, and 2.14%, respectively. The size of these core samples is two inches in length and one inch in diameter. Specifically, in the sample labels, "PL" denotes that the core axis direction is parallel to the bedding plane direction, whereas "PD" indicates that the core axis direction is perpendicular to the bedding plane direction.

3. Theories and experimental equipment

3.1. The Klinkenberg equation

It is the Klinkenberg effect that leads to the difference between apparent permeability and absolute (intrinsic) permeability, especially under low pore pressures. In order to quantify the Klinkenberg effect, the Klinkenberg coefficient (Klinkenberg, 1941) was used to describe the role of pore pressure on the apparent permeability. The Klinkenberg coefficient depends on the petrophysical properties of the rock, and is included in the Klinkenberg equation written as follows:

$$\frac{k_a}{k} = 1 + \frac{b}{P_p} \tag{1}$$

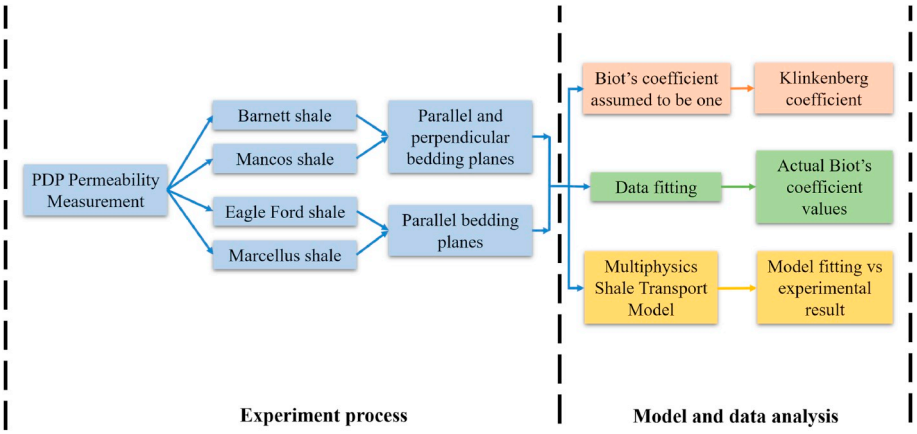

Fig. 1. Overview of the experiment and modeling workflow for the assessment of the correlations between apparent permeability, confining pressure, and pore pressure.

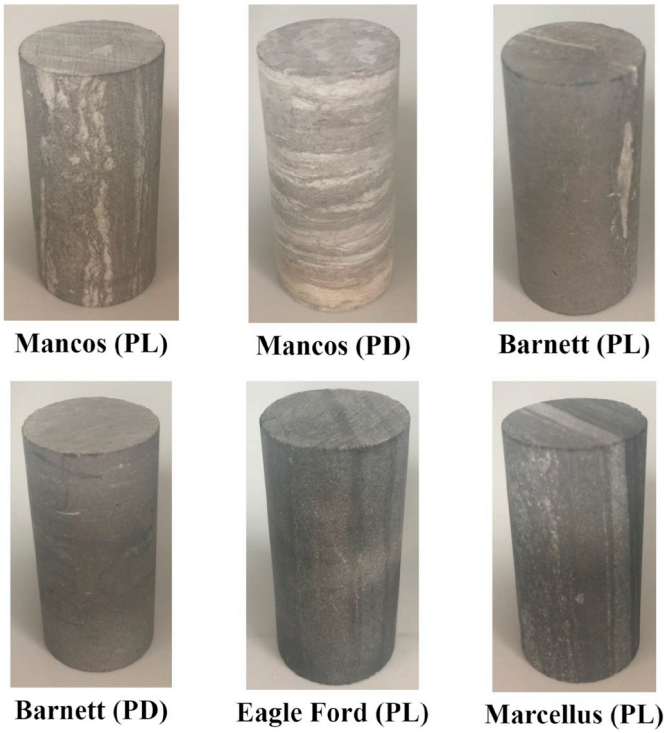

Fig. 2. Overview of the shale cores used in the PDP tests, which were extracted from four U.S. shale formations including the Eagle Ford, Marcellus, Mancos, and Barnett formations. In the sample names, "PL" denotes that the core axis direction is parallel to the bedding plane direction, whereas "PD" indicates that the core axis direction is perpendicular to the bedding plane direction.

where k_a is the apparent permeability (m^2), P_p is the pore pressure (Pa), k is the absolute permeability of the porous medium (m^2), and b is the Klinkenberg coefficient (Pa), which can be calculated based on the analysis of the mass fluxes contributed by the viscous flow and Knudsen diffusion. In this study, we focus on the nanopores that have planar geometry because the MPST model is in the two-dimensional (2D) space, as will be described in Section 4. In addition, the width of a planar nanopore is sensitive to the stress applied in the direction perpendicular to the planar pore walls, which is the foundation of the MPST model because one of the primary applications of the MPST model is to describe the response of the apparent permeability to the change of effective stress.

Mass flux through a planar nanopore can be written as:

$$J = J_D + J_K \tag{2}$$

where J_D is the mass flux resulting from Darcy flow ($kg/m^2/s$), which is the viscous flow driven by a pressure gradient through the nanopore; J_K is the mass flux resulting from Knudsen diffusion ($kg/m^2/s$), which occurs when the nanopore width is comparable to or smaller than the mean-free-path length of gas molecules.

The value of J_D can be calculated using the Darcy's law:

$$J_D = -\frac{k}{\mu}\rho\nabla p \tag{3}$$

where μ is dynamic viscosity (Pa s); ρ is free gas mass density (kg/m^3); ∇p is the pressure gradient through the nanopore (Pa/m). In a planar nanopore, one can analytically solve the Navier-Stokes equations to calculate the absolute permeability as $k = h^2/12$, where h is the width of the planar nanopore (m). However, in nanometer-scale pores, the no-slip boundary condition is invalid and thus a dimensionless coefficient, F, must be used to account for the enhancement of mass flux resulting from the slip boundary condition (Brown et al., 1946). Therefore, mass flux through a planar nanopore resulting from Darcy flow is calculated as:

$$J_D = -F\frac{h^2}{12\mu}\rho\nabla p \tag{4}$$

where F is the dimensionless coefficient and calculated as:

$$F = 1 + \frac{2\mu}{ph}\left(\frac{2}{\alpha} - 1\right)\sqrt{\frac{8\pi RT}{M}} \tag{5}$$

where p is pressure (Pa); α is the tangential momentum accommodation coefficient having a value in the range from 0 to 1; R is the gas constant and equal to 8.314 J/mol/K; T is absolute temperature (K); M is molar mass (kg/mole).

Mass flux contributed by Knudsen diffusion, J_K, is calculated as:

$$J_K = -\frac{MD_K}{RT}\nabla p \tag{6}$$

where D_K is the Knudsen diffusivity (m^2/s) calculated as:

$$D_K = \frac{h}{3}\sqrt{\frac{8RT}{\pi M}} \tag{7}$$

Substituting Equations (4) and (6) into Equation (2) and using Equations (5) and (7), one can re-write Equation (2) as follows:

$$J = -\left[\left(1+\frac{2\mu}{ph}\left(\frac{2}{\alpha}-1\right)\sqrt{\frac{8\pi RT}{M}}\right)\frac{\rho h^2}{12\mu}+\frac{hM}{3RT}\sqrt{\frac{8RT}{\pi M}}\right]\nabla p \tag{8}$$

Equation (8) can be re-written in the form of the Darcy's law:

$$J = -\frac{k_a}{\mu}\rho\nabla p \tag{9}$$

where k_a is the apparent permeability that accounts for the mass flux contributions from both slip boundary and Knudsen diffusion. Comparing Equation (8) with 9, one obtains:

$$k_a = \left(1+\frac{2\mu}{ph}\left(\frac{2}{\alpha}-1\right)\sqrt{\frac{8\pi RT}{M}}\right)\frac{h^2}{12}+\frac{hM\mu}{3RT\rho}\sqrt{\frac{8RT}{\pi M}} \tag{10}$$

By normalizing k_a with $k = h^2/12$ and using $\rho = \frac{PM}{RT}$, one obtains:

$$\frac{k_a}{k} = 1+\frac{2\mu}{ph}\left(\frac{2}{\alpha}-1\right)\sqrt{\frac{8\pi RT}{M}}+\frac{4\mu}{ph}\sqrt{\frac{8RT}{\pi M}} \tag{11}$$

By comparing Equation (11) with the Klinkenberg equation (Equation (1)), one obtains the formula for calculating the Klinkenberg coefficient in a planar nanopore:

$$b = \frac{2\mu}{h}\left(\frac{2}{\alpha}-1\right)\sqrt{\frac{8\pi RT}{M}}+\frac{4\mu}{h}\sqrt{\frac{8RT}{\pi M}} \tag{12}$$

Calculation of the Biot's coefficient using pressure pulse decay experiments.

The Biot's coefficient is a poroelastic parameter that described the influence of the pore pressure on the effective stress (Bernabe, 1986):

$$P_e = P_c - \chi P_p \tag{13}$$

where P_e is effective stress (Pa), P_c is confining pressure (Pa), P_p is pore pressure (Pa), and χ is the Biot's coefficient, of which the value depends on the rock's mineral composition. Equation (13) suggests that the confining pressure and pore pressure have different influences on the effective stress if the value of χ is not equal to one.

Because P_e is a function of P_p and P_c, the apparent (measured) permeability, k_a, can be written as a function of these two variables:

$$k_a = k_a(P_c, P_p) \tag{14}$$

In this study, log(k) (Chen and Zeng, 2015) is used as an indicator of the formation permeability:

$$log(k_a) = log(k_a)(P_c, P_p) \tag{15}$$

Based on Equation (15), one obtains the differential of log(k):

$$dlog\left(k_a\right) = \left(\frac{\partial log(k_a)}{\partial P_c}\right)dP_c + \left(\frac{\partial log(k_a)}{\partial P_p}\right)dP_p \tag{16}$$

One also has the following equation based on Equation (13):

$$dP_e = dP_c - \chi dP_p \tag{17}$$

When the effective stress stays constant, both dlog (k_a) and dP_e are zero. Therefore, one obtains the following two equations based on Equations (16) and (17):

$$\left(\frac{\partial log(k_a)}{\partial P_c}\right)dP_c + \left(\frac{\partial log(k_a)}{\partial P_p}\right)dP_p = 0 \tag{18}$$

and

$$dP_c - \chi dP_p = 0 \tag{19}$$

Using Equations (18) and (19), one obtains:

$$\chi = -\left(\frac{\partial \log(k_a)}{\partial P_p}\right) \Big/ \left(\frac{\partial \log(k_a)}{\partial P_c}\right) \tag{20}$$

3.2. Pulse decay permeameter experiments

The PDP equipment is a transient, time-effective approach to measuring the apparent permeability of tight rocks. Jones (1997) developed the basic measurement principle of PDP and found that the measurement range of PDP is from 0.1 mD to 0.01 microdarcy (μD). As opposed to traditional permeability measurement methods, which use flow parameters in the steady state and are based on Darcy's law, the PDP method uses transient flow parameters, which significantly accelerates the measurement process and consequently is ideal for low-permeability rocks. Our PDP experiments were conducted under a fixed indoor temperature of 20 °C. Fig. 3 is a schematic plot of the PDP setup. The testing gas used in the PDP is pure nitrogen. The pore pressure is controlled using a pressure regulator, whereas the confining pressure is controlled using a hydraulic pump. The flow rate measurement is not required but can be calculated from the known volumes of the reservoirs, fluid compressibility, and the rate of change of gas pressures (Hsieh et al., 1981; Bourbie and Walls, 1982). In the PDP testing, the pore pressure, P_p, throughout the core sample is uniform in the initial stage. When $t = 0$, a gas pressure slightly higher than the initial pore pressure is applied at the upstream end of the core sample. When the pressure pulse propagates through the core sample, the gas pressure in the downstream reservoir increases whereas the gas pressure in the upstream reservoir declines. After a certain period of time, the pressure difference between the upstream and downstream reservoirs approaches zero. The decay rate of this pressure difference is proportional to the permeability of the core sample. Dicker and Smits (1988) developed the general analytical solution of the differential pressure as a function of time. Chen and Stagg (1984) and Haskett et al. (1988) also made contributions to the analytical solutions.

4. Multi-physics shale transport model

Recent studies by the authors (Chen et al., 2013; Chen, 2016) showed that the pore and fracture size distribution and associated gas transport in shale formations have a hierarchical structure and thus demonstrate multi-scale properties. Based on previous investigations, a MPST model was developed in this paper to account for the coupled multi-physics processes of fluid dynamics, geomechanics, and the Klinkenberg effect in shale gas transport. Fig. 4 illustrates the hierarchical geometry structure in the MPST model. Specifically, pore pressure, P_p, and effective stress, P_e, are the two independent input variables in this MPST model, and the rock's overall apparent permeability, $\bar{k}_a$, is the model output. Fig. 4 demonstrates that a 2D shale gas formation consists of two transport domains: kerogen and inorganic matrix (Chen, 2016). The two domains have their own intrinsic permeabilities, mechanical

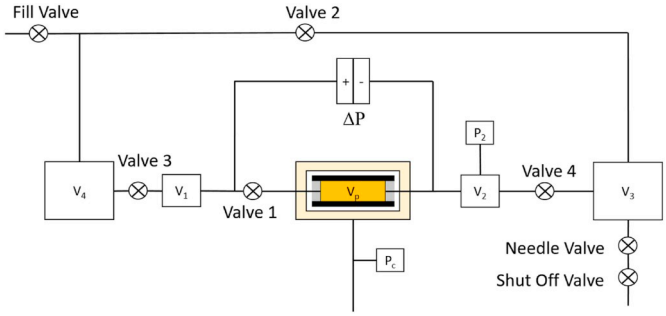

Fig. 3. Schematic PDP equipment setup, which consists of an upstream test gas reservoir having a volume of V_1, a high-pressure core holder with the pore volume of V_p in the sample, a downstream gas reservoir having a volume of V_2, a differential pressure transducer to continuously measure the pressure difference (ΔP) between the upstream and downstream reservoirs, and a second pressure transducer to measure the downstream reservoir pressure, P_2. This picture is from Core Lab PDP-200 operations manual.

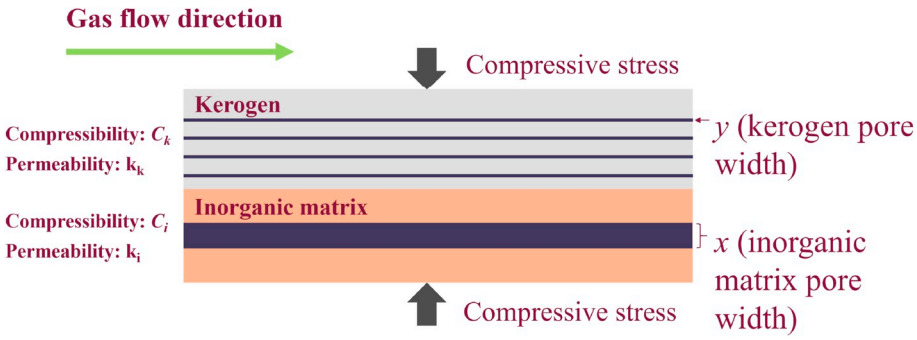

Fig. 4. Schematic picture illustrating the two transport domains in the MPST model: kerogen and inorganic matrix. The entire shale gas rock is subjected to compressive stress due to the confining pressure. The single pore width in the kerogen domain is equal to y, whereas the single pore width in the inorganic matrix is equal to x. The pore width in the inorganic matrix is in general much larger than that in the kerogen domain. The kerogen pores and inorganic matrix pores have a number ratio of N.

compressibilities, and pore widths. The entire shale gas rock is subjected to compressive stress due to the confining pressure. The single pore width (m) in the kerogen domain is equal to *y*, whereas the single pore width (m) in the inorganic matrix is equal to *x*. The pore width in the inorganic matrix is in general much larger than that in the kerogen domain. The kerogen pores and inorganic matrix pores have a number ratio of *N*, which implies that the number of kerogen pores is *N* times of the number of inorganic matrix pores.

Based on Equation (1), the apparent permeabilities of a single inorganic matrix pore and a single kerogen pore can be calculated as:

$$k_i = \frac{x^2}{12}\left(1 + \frac{b(x)}{P}\right)$$
$$k_k = \frac{y^2}{12}\left(1 + \frac{b(y)}{P}\right) \tag{21}$$

where $b(x)$ and $b(y)$ are the Klinkenberg coefficients in the inorganic matrix and kerogen, respectively. The output of the MPST model is the measured overall permeability of the entire shale gas rock, which can be calculated as follows using the Darcy's law:

$$\bar{k} = \frac{\bar{u}\cdot\mu}{\nabla P} = \frac{(Q_i + Q_k)\mu}{A\cdot\nabla P} \tag{22}$$

where A is the total cross section area (m^2) through which the gas flows and is calculated as $A = \frac{x+N\cdot y}{\varphi}$, where φ is the total porosity of the rock. $\bar{u}$ is the average flow velocity across the entire cross section area and is calculated as $\bar{u} = \frac{Q_i+Q_k}{A}$, where Q_i and Q_k are the gas flow rates contributed by the inorganic matrix domain and the kerogen domain, respectively. Specifically, Q_i and Q_k can be calculated as follows:

$$Q_i = u_i\cdot x = \frac{k_i}{\mu}\cdot\nabla P\cdot x = \frac{x^3}{12}\cdot\frac{\nabla P}{\mu}\left(1 + \frac{b(x)}{P}\right)$$
$$Q_k = Nu_k\cdot y = \frac{Nk_k}{\mu}\cdot\nabla P\cdot y = \frac{Ny^3}{12}\cdot\frac{\nabla P}{\mu}\left(1 + \frac{b(y)}{P}\right) \tag{23}$$

The Klinkenberg coefficients for the planar pores in the inorganic matrix domain and kerogen domain in the MPST model can be calculated using Equation (12):

$$b(x) = \frac{2\mu}{x}\left(\frac{2}{\alpha} - 1\right)\sqrt{\frac{8\pi RT}{M}} + \frac{4\mu}{x}\sqrt{\frac{8RT}{\pi M}}$$
$$b(y) = \frac{2\mu}{y}\left(\frac{2}{\alpha} - 1\right)\sqrt{\frac{8\pi RT}{M}} + \frac{4\mu}{y}\sqrt{\frac{8RT}{\pi M}} \tag{24}$$

The pore widths in Equation (24), x and y, depend on the effective stress and can be calculated as follows:

$$x = x_0[1 - C_i\Delta P_e]$$
$$y = y_0[1 - C_k\Delta P_e] \tag{25}$$

where x_0 and y_0 are the initial (reference) pore widths in the inorganic matrix and kerogen domains, respectively; ΔP_e is the change of the effective stress compared to the effective stress in the reference state; C_i and C_k are the compressibility coefficients of the inorganic matrix pore and kerogen pore, respectively, which reflect the responses of the pore width to the change of the effective stress.

In addition, the porosity of the entire shale rock can be calculated as:

$$\varphi = \frac{x + Ny}{x + Ny + S} = \frac{x_0[1 - C_i\Delta P_e] + Ny_0[1 - C_k\Delta P_e]}{x_0[1 - C_i\Delta P_e] + Ny_0[1 - C_k\Delta P_e] + S} \tag{26}$$

where S is the cross-section width contributed by the solids.

Substituting Equations (23)–(26) into Equation (22), one can rewrite Equation (22) as follows:

$$\bar{k} = \frac{x_0[1 - C_i\Delta P_e] + Ny_0[1 - C_k\Delta P_e]}{x_0[1 - C_i\Delta P_e] + Ny_0[1 - C_k\Delta P_e] + S} \cdot \frac{x_0^3(1 - C_i\Delta P_e)^3\left[1 + \frac{2\mu\left(\frac{2}{\alpha}-1\right)\sqrt{\frac{8\pi RT}{M}} + 4\mu\sqrt{\frac{8RT}{\pi M}}}{x_0(1 - C_i\Delta P_e)P_p}\right] + Ny_0^3(1 - C_k\Delta P_e)^3\left[1 + \frac{2\mu\left(\frac{2}{\alpha}-1\right)\sqrt{\frac{8\pi RT}{M}} + 4\mu\sqrt{\frac{8RT}{\pi M}}}{y_0(1 - C_k\Delta P_e)P_p}\right]}{12[x_0(1 - C_i\Delta P_e) + Ny_0(1 - C_k\Delta P_e)]} \tag{27}$$

Equation (27) provides a detailed formulation for the MPST model, which predicts the overall apparent permeability of the shale gas sample, $\bar{k}$, as the model output by accounting for the multi-physics processes of fluid dynamics, geomechanics, and the Klinkenberg effect. Specifically, the MPST model takes two independent input variables on the right-hand side of Equation (27), which are the effective stress change, ΔP_e, and the pore pressure, P_p.

5. Results and discussion

Fig. 5 illustrates the PDP-measured apparent permeability as a function of pore pressure under different effective stresses. The solid curves are the MPST model fitting curves based on the PDP experimental data points. In this figure, the effective stresses were calculated based on

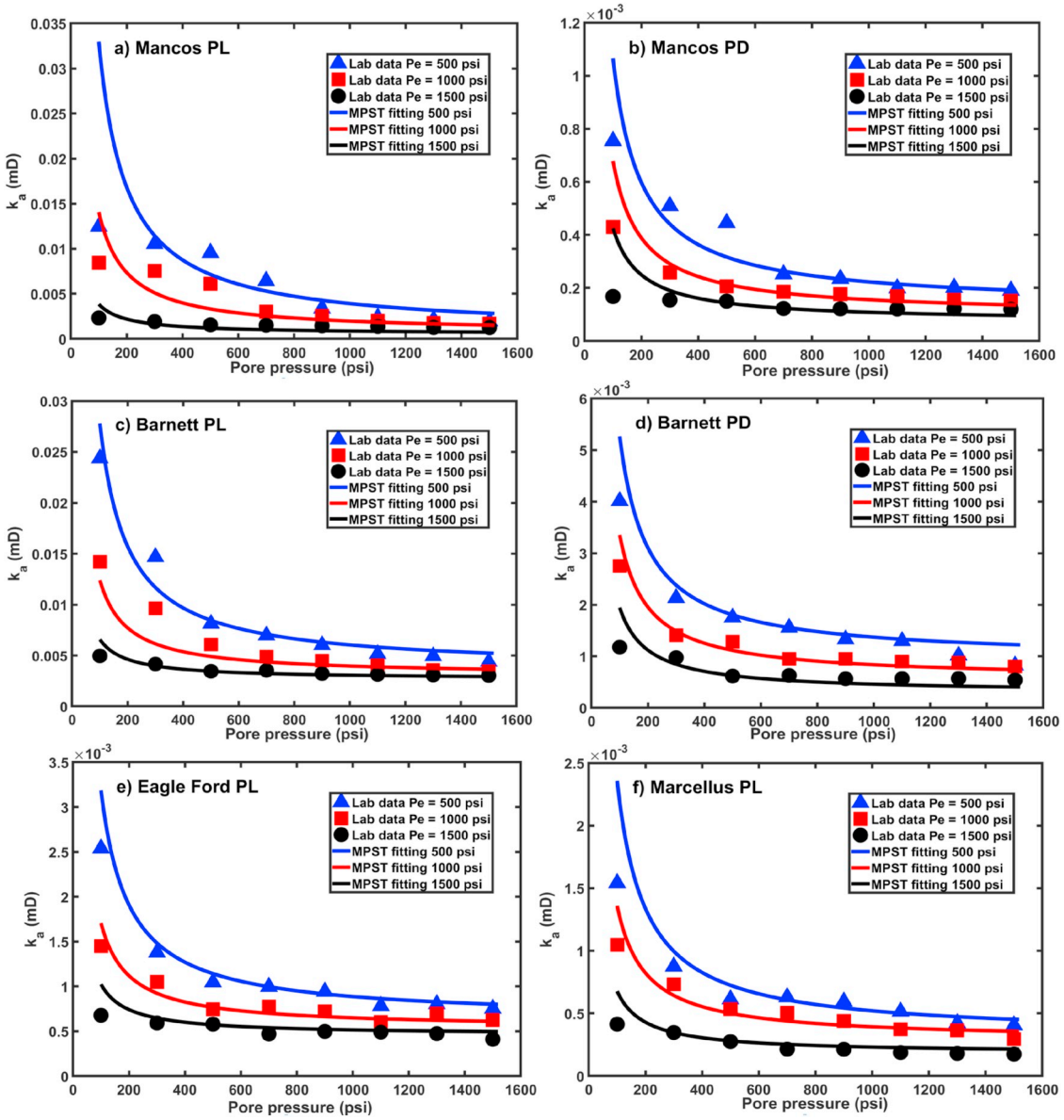

Fig. 5. Apparent permeability measured in the PDP experiments as a function of pore pressure under different effective stresses in the core samples of a) Mancos PL, b) Mancos PD, c) Barnett PL, d) Barnett PD, e) Eagle Ford PL, and f) Marcellus PL. The solid curves are the MPST model fitting curves based on the scattered PDP experimental data points.

the assumption that the Biot coefficient is one for the sake of simplicity. This is because calculation of the actual Biot coefficient value using Equation (20) requires comprehensive laboratory tests of the same core sample under various combinations of pore and confining pressures, which can be time consuming using the PDP equipment and might cause the development of microfractures in the core sample due to the cyclic loading and unloading processes in the PDP. Therefore, in many applications when no other information is available, the Biot's coefficient is usually assumed to be one (Alam et al., 2014; and Bhandari et al., 2015; Jin et al., 2015; Rydzy et al., 2016). All six groups of the PDP tests demonstrated that the apparent permeability decreased with increasing pore pressure. The sample of Mancos PL had the highest average permeability across all pore pressures, whereas the sample of Mancos PD had the lowest average permeability. Because high pore pressure mitigates the Klinkenberg effect (Vermylen, 2011), in this study the average value of the apparent permeabilities at the pore pressures of 1300 psi and 1500 psi were considered as the absolute permeability of the core. Soeder (1988) used laboratory tests to measure apparent permeability under varying pore pressures for cores extracted from the Marcellus shale, and found that when the pore pressure was higher than 500 psi permeability change was smaller than 15%, which is consistent with our finding. Therefore, the apparent permeabilities measured under 1300 psi and 1500 psi were very close to the absolute permeability. It was found that the absolute permeabilities of all core samples ranged from 10^{-4} mD to 10^{-2} mD. In addition, it was noticed that in the same shale formation the permeabilities in the cores where the bedding planes were parallel to the core axis were approximately one order of magnitude higher than those in the cores where the bedding planes were perpendicular to the core axis. This is because the pore spaces between bedding planes have higher connectivity and thus provide higher gas flow conductivity, leading to higher permeability if the sample is cored in this direction.

Fig. 5 illustrates that the effective stress is a critical input variable in the MPST model, which has a great impact on the PDP-measured apparent permeability. Under high effective stress (1500 psi), the apparent permeability did not noticeably change when the pore pressure

increased, which suggests that the Klinkenberg effect is mitigated. This is because for most core samples there exists connected pore networks having various spatial scales. The relatively small pore networks are more sensitive to effective stress and they shut off when the effective stress increases, leaving relatively large pore networks open, which are relatively insensitive to the Klinkenberg effect and thus have relatively smaller Klinkenberg coefficients. When the effective stress was 500 psi, the apparent permeabilities decreased noticeably with increasing pore pressure, suggesting that the Klinkenberg effect is significant under the relatively low effective stress because all relatively small pore networks stay open, which are subjected to noticeable Klinkenberg effect.

The PDP experimental data were fitted to the MPST model, and the fitting curves demonstrated that the MPST model successfully captured the influences of pore pressure and effective stress on the measured apparent permeability. During the data fitting processes, we found that the magnitude of the apparent permeability is controlled primarily by the pore widths, x and y, and the solid section width, S, whereas the shape of the curve (curvature) is controlled primarily by the kerogen and inorganic matrix compressibility coefficient, C_k and C_i.

Fig. 6 illustrates k_a/k as a function of $1/P_p$, as well as the linear equation fitting lines. Based on Equation (1), the y-intercept of the linear equation is 1, and the slope is equal to the Klinkenberg coefficient, b. The variation of the value of b as a function of the effective stress was consistent with the observation in Fig. 5. It was also noticed that most values of b fell into the range between 100 psi and 400 psi, which were close to what were found in the literature based on experimental (Soeder, 1988) and analytical (Chen, 2016) methods.

In the next step, the data fitting method, which was originally developed by Bernabe (1986) and then improved by Kwon et al. (2001), was utilized to determine the actual value of the Biot's coefficient using Equation (20). Fig. 7 illustrates log (k_a) as a function of the confining pressure, P_c, under varying pore pressures. The slope of the fitted straight lines was equal to $\partial \log (k_a)/\partial P_c$. Based on the method of Kwon et al. (2001), the value of $\partial \log (k_a)/\partial P_c$ in the same core sample should be constant and independent of the specific pore pressure value, which is confirmed in Fig. 7. Therefore, in this study the data measured under the pore pressure of 1500 psi was used to determine $\partial \log (k_a)/\partial P_c$. It should be noted that in the same core sample the slopes of the straight lines fitted under the other pore pressures were close to that for the pore pressure of 1500 psi. Fig. 7 demonstrates that the value of $\partial \log (k_a)/\partial P_c$ ranges from -4×10^{-5} to -4×10^{-4}.

Fig. 8 illustrates log (k_a) as a function of the pore pressure, P_p, under varying confining pressures. The slope of the fitted straight lines was equal to $\partial \log (k_a)/\partial P_p$. Based on the method of Kwon et al. (2001), the value of $\partial \log (k_a)/\partial P_p$ in the same core sample should be constant and independent of the specific confining pressure value, which is confirmed

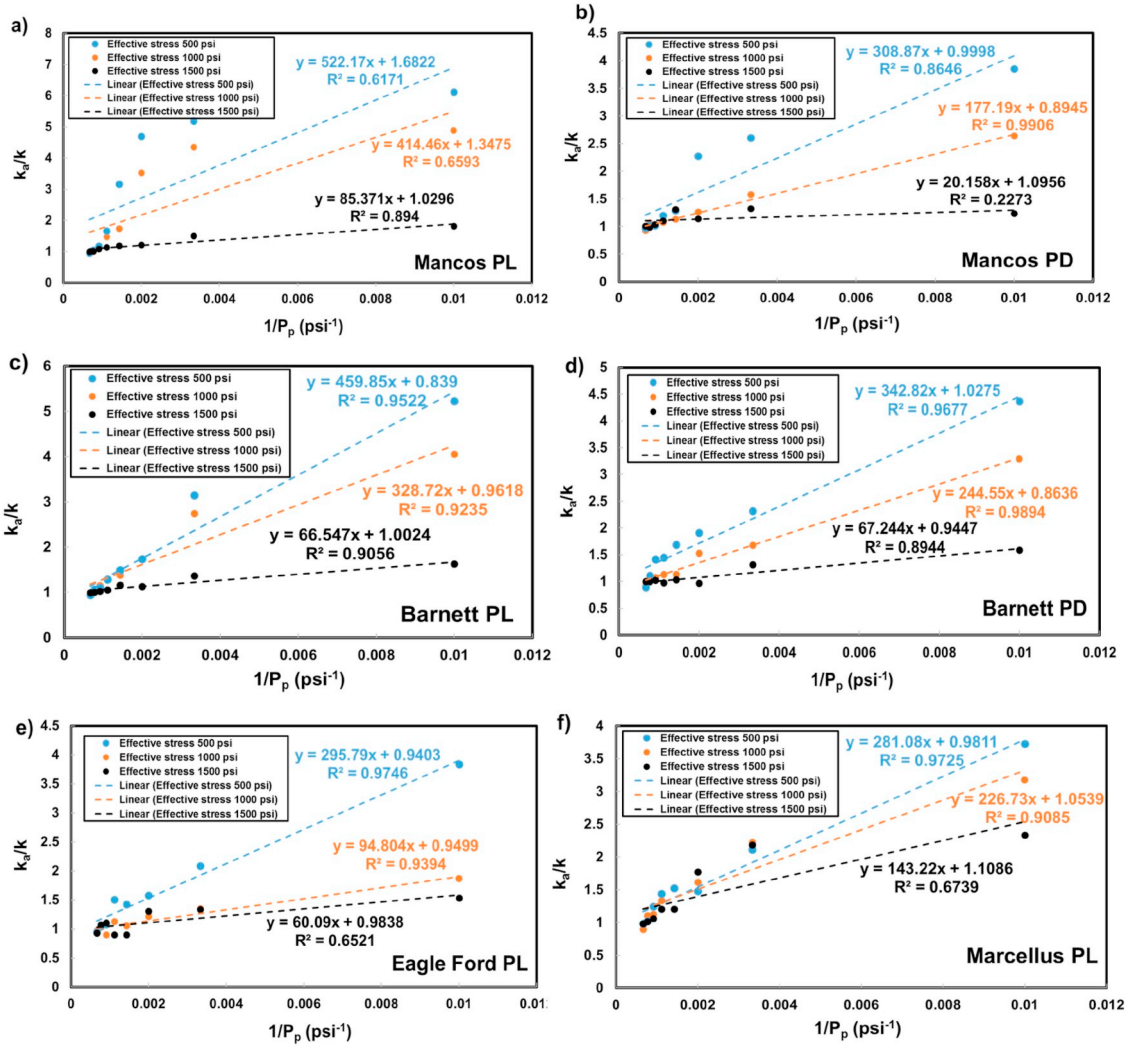

Fig. 6. k_a/k as a function of $1/P_p$, as well as the linear equation fitting lines, in the core samples of a) Mancos PL, b) Mancos PD, c) Barnett PL, d) Barnett PD, e) Eagle Ford PL, and f) Marcellus PL. In the figure legend, "linear" refers to the linear fitting lines. Based on Equation (1), the slope of the fitting line is equal to the Klinkenberg coefficient, b.

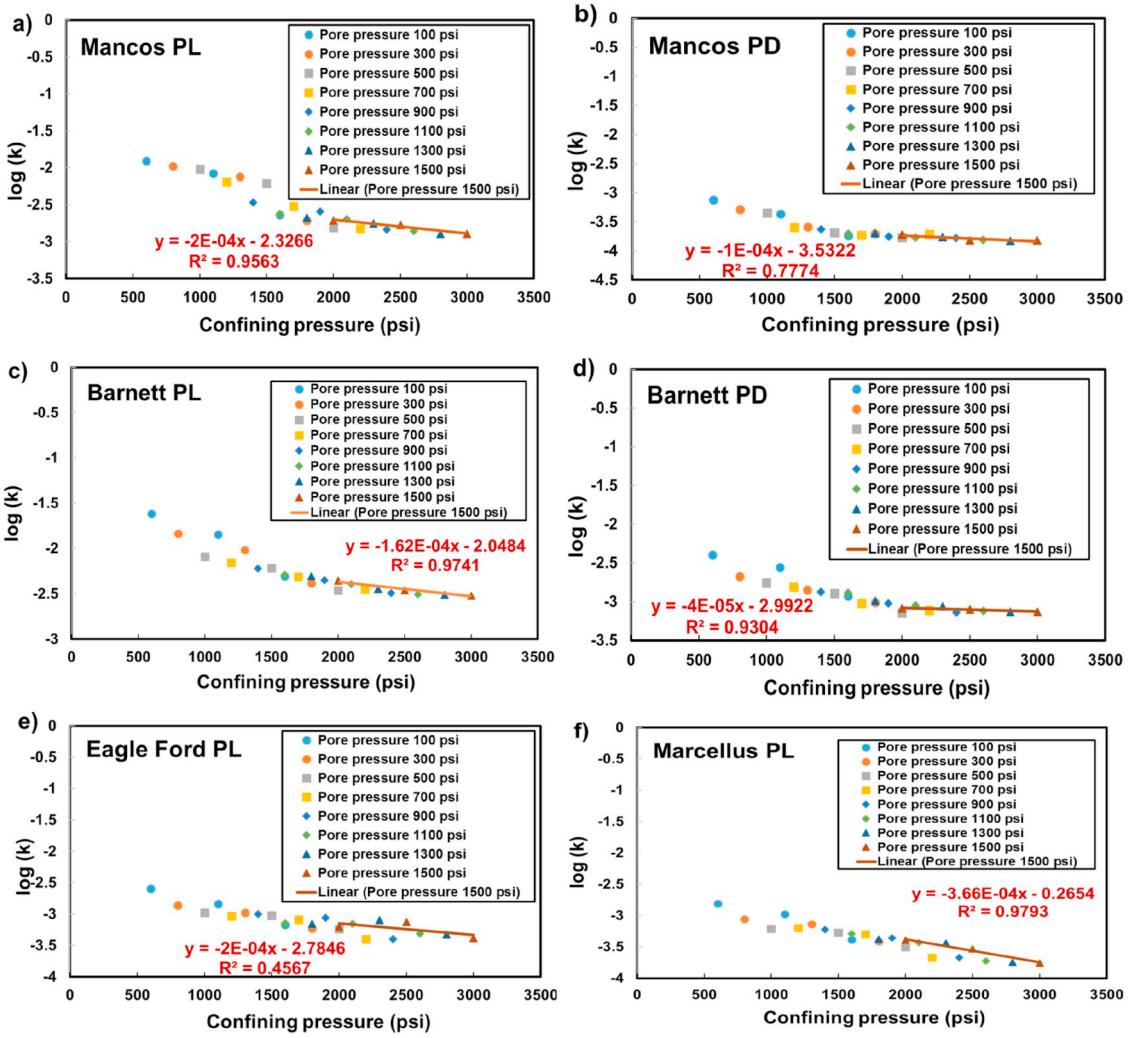

Fig. 7. The value of log (k_a) as a function of the confining pressure, P_c, under varying pore pressures in the formations of a) Mancos PL, b) Mancos PD, c) Barnett PL, d) Barnett PD, e) Eagle Ford PL, and f) Marcellus PL. In the figure legend, "linear" refers to the linear fitting lines.

in Fig. 8. Thus, in this study the data measured under the confining pressure of 2000 psi was used to fit $\partial \log (k_a)/\partial P_p$. In the same core sample, the slopes of the straight lines fitted under the other confining pressures were close to that for the confining pressure of 2000 psi. Fig. 8 demonstrates that the value of $\partial \log (k_a)/\partial P_p$ ranges from 2×10^{-5} to 1×10^{-4}.

Based on the results from Figs. 7 and 8, the values of the Biot's coefficient, χ, in the six shale formations were calculated using Equation (20). Specifically, the values of χ were 0.50, 0.50, 0.62, 0.50, 0.35 and 0.26, for Mancos PL, Mancos PD, Barnett PL, Barnett PD, Eagle Ford PL, and Marcellus PL, respectively. Other researchers (da Silva et al., 2008; Gutierrez et al., 2015) found similar Biot coefficient values in shale. These relatively low values of the Biot's coefficient in shale suggest that the pore pressure had a lesser influence on the effective stress compared to the confining pressure. The Biot's coefficient in the shale is greatly impacted by the clay minerals content, fluid-filled pore geometries, and homogeneous elastic properties. Because the shale is known for its heterogeneity, it is usually treated as a composite material. Therefore, each shale formation has its unique property, which explains the scattered values in the calculated Biot's coefficient.

6. Conclusions

In this study, comprehensive core analyses using PDP laboratory testing were conducted to investigate the relationships between apparent permeability, pore pressure, and confining pressure. The influence of the Klinkenberg effect and the role of the bedding planes direction on the PDP-measured apparent permeabilities were studied. Based on the large volume of PDP experimental data, the actual values of the Biot's coefficient were determined by data fitting. The laboratory results indicate that in the same shale formation the permeabilities of the cores in which the bedding planes were parallel to the core axis were approximately one order of magnitude higher than those in the cores in which the bedding planes were perpendicular to the core axis. Under higher effective stresses, the apparent permeability did not change noticeably when the pore pressure increased. This was because that for most core samples there exist connected pore networks having heterogeneous spatial scales (i.e., a wide range of pore size distribution). The relatively small pore networks are more sensitive to effective stress and they are isolated when the effective stress increases, leaving relatively large pore networks open, which are relatively insensitive to the Klinkenberg effect and thus have relatively small Klinkenberg coefficients.

The MPST model is developed to account for the coupled multi-physics processes of geomechanics, fluid dynamics, and the Klinkenberg effect for gas transport in shales. Specifically, this novel model takes into account the fluid dynamics associated with gas transport in organic and inorganic pores, compression of both kerogen (organic matters) and inorganic matrix under stress, and the Klinkenberg effect. In the MPST model, pore pressure and effective stress are the two independent input variables, whereas the measured apparent permeability

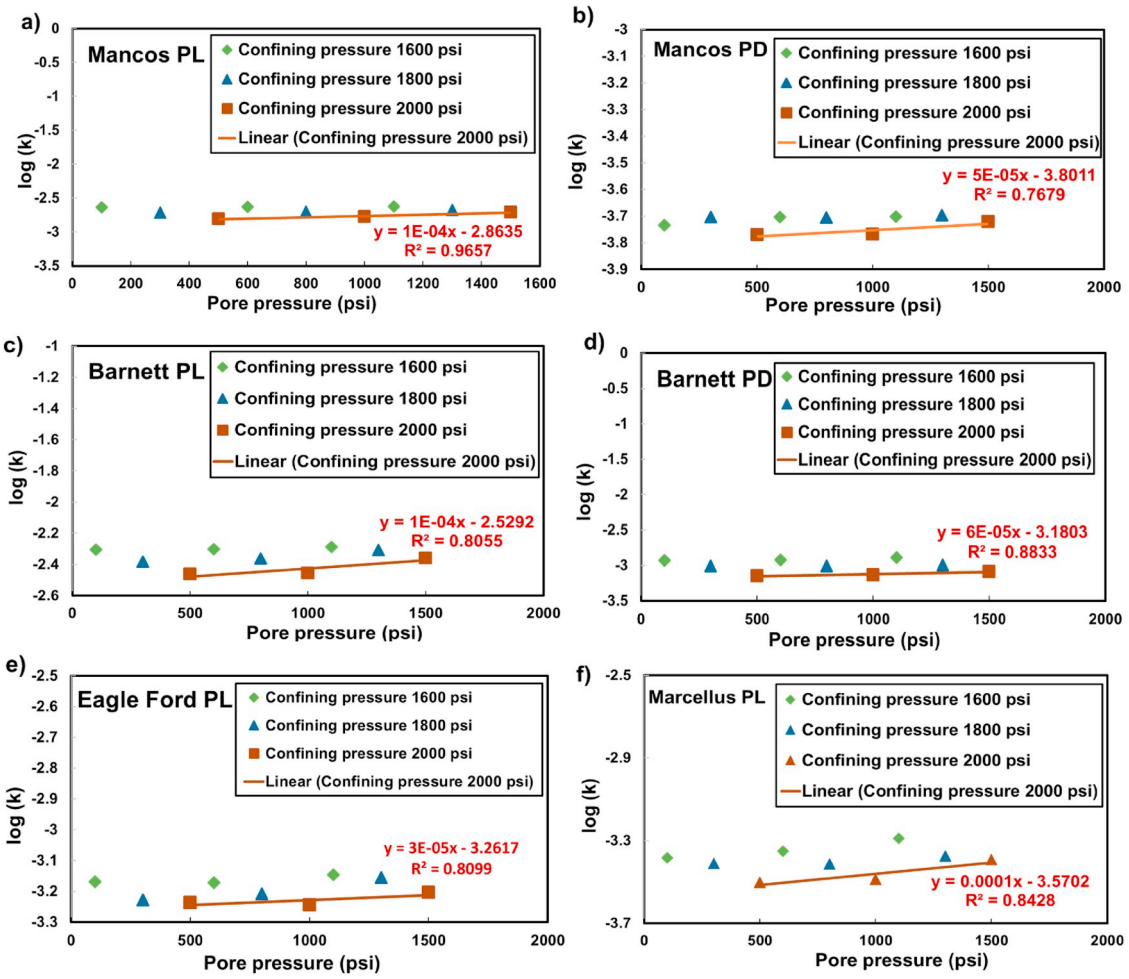

Fig. 8. The value of log (k_a) as a function of pore pressure, P_p, in the formations of a) Mancos PL, b) Mancos PD, c) Barnett PL, d) Barnett PD, e) Eagle Ford PL, and f) Marcellus PL. In the figure legend, "linear" refers to the linear fitting lines.

is the model output. In this study, the PDP experimental data were fitted to the MPST model, and the fitting curves showed that the MPST model successfully captures the influence of both pore pressure and effective stress on the apparent permeability.

The MPST model development aims to answer the question if it is possible to predict and fit laboratory data for the apparent permeability of a shale using pore pressure and effective stress change as model inputs. The result from this work demonstrates that the MPST model is a simple but effective framework to interpret laboratory PDP data measured under various confining and pore pressures and it is able to account for the multi-physics processes of geomechanics, fluid dynamics, and the Klinkenberg effect that all affect the measured apparent permeability for gas transport in shales. This study advances the fundamental understanding of the role of confining pressure, pore pressure, Klinkenberg effect, and bedding plane direction on the apparent permeability of shales. Therefore, The MPST model has practical applications to assess the apparent permeability in a shale gas formation under specified pore pressure and effective stress, which is crucial in accurately predicting the recovery factor and recovery rate using reservoir simulations (e.g., Chen, 2016). The research outcome has the potential to benefit the optimization of engineering designs in horizontal wells in shales including hydraulic fracturing, re-stimulation, and optimal well landing location. The laboratory experiments provide insights into the Klinkenberg effect and its role on the apparent permeability under varying confining and pore pressures in different U. S. shale formations.

Declaration of competing interest

There is no conflict of interest associated with this manuscript.

Acknowledgement

The authors are thankful to the funding support of the Junior Faculty Award from Virginia Tech's Institute for Critical Technology and Applied Science, as well as the financial assistance provided by the U.S. Department of Energy through the National Energy Technology Laboratory under Contract No. DE-FE0031576.

Appendix A. Supplementary data

Supplementary data to this article can be found online at https://doi.org/10.1016/j.petrol.2020.107010.

Nomenclature

A	model total width
b	Klinkenberg coefficient
C_k	kerogen compressibility
C_i	inorganic matrix compressibility
d	pore diameter
k	absolute permeability
$\overline{k}$	model apparent permeability
k_a	apparent permeability
k_i	inorganic matrix permeability
k_k	kerogen permeability
Kn	Knudsen number
L	model length
M	molar mass
N	number ratio
P_c	confining pressure
P_e	effective stress
P_p	pore pressure
Q_i	flow rate in the inorganic matrix
Q_k	flow rate in the kerogen
r	effective pore radius
R	gas constant
S	solid section width
T	absolute temperature
t	time
$\overline{u}$	average flow velocity
u_k	kerogen flow velocity
u_i	inorganic matrix flow velocity
x	kerogen fracture width
x_0	reference width of x
y	inorganic matrix fracture width
y_0	reference area of y
φ	total porosity
χ	Biot's coefficient
α	tangential momentum accommodation coefficient
λ	free gas mean-free-path length
μ	dynamic viscosity
ρ	free gas mass density

References

Alam, A.B., Niioka, M., Fujii, Y., Fukuda, D., Kodama, J.I., 2014. Effects of confining pressure on the permeability of three rock types under compression. Int. J. Rock Mech. Min. Sci. 65, 49–61.

Bernabe, Y., 1986. The effective pressure law for permeability in Chelmsford granite and Barre granite. Int. J. Rock Mech. Min. Sci. Geomech. Abstr. 23 (3), 267–275 (Pergamon).

Beskok, A., Karniadakis, G.E., 1999. A model for flows in channels, pipes, and ducts at micro and nano scales. Microscale Thermophys. Eng. 3, 43–77.

Bhandari, A.R., Flemings, P.B., Polito, P.J., Cronin, M.B., Bryant, S.L., 2015. Anisotropy and stress dependence of permeability in the Barnett shale. Transport Porous Media 108 (2), 393–411.

Blanchard, V., Lasseux, D., Bertin, H.J., Pichery, T.R., Chauveteau, G.A., Tabary, R., Zaitoun, A., 2007. Gas/water flow in porous media in the presence of adsorbed polymer: experimental study on non-Darcy effects. SPE Reservoir Eval. Eng. 10 (4), 423–431.

Bourbie, T., Walls, J., 1982. Pulse decay permeability: analytical solution and experimental test. Soc. Petrol. Eng. J. 22 (5), 719–721.

Brown, G.P., Dinardo, A., Cheng, G.K., Sherwood, T.K., 1946. The flow of gases in pipes at low pressures. J. Appl. Phys. 17, 802–813.

Chen, C., 2016. Multiscale imaging, modeling, and principal component analysis of gas transport in shale reservoirs. Fuel 182, 761–770.

Chen, C., Hu, D., Westacott, D., Loveless, D., 2013. Nanometer-scale characterization of microscopic pores in shale kerogen by image analysis and pore-scale modeling. G-cubed 14 (10), 4066–4075.

Chen, C., Martysevich, V., O'Connell, P., et al., 2015a. Temporal evolution of the geometrical and transport properties of a fracture/proppant system under increasing effective stress. SPE J. 20 (3), 527–535. https://doi.org/10.2118/171572-PA. SPE-171572-PA.

Chen, C., Zeng, L., 2015. Using the level set method to study the effects of heterogeneity and anisotropy on hyporheic exchange. Water Resour. Res. 51, 3617–3634. https://doi.org/10.1002/2014WR016444.

Chen, C., Wang, Z., Majeti, D., Vrvilo, N., Warburton, T., Sarkar, V., Li, G., 2016. Optimization of lattice Boltzmann simulation with graphics-processing-unit parallel computing and the application in reservoir characterization. SPE J. 21 (4), 1–425.

Chen, D., Pan, Z., Ye, Z., 2015b. Dependence of gas shale fracture permeability on effective stress and reservoir pressure: model match and insights. Fuel 139, 383–392.

Chen, T., Stagg, P.W., 1984. Semilog analysis of the pulse-decay technique of permeability measurement. Soc. Petrol. Eng. J. 24 (6), 639–642.

Cui, G., Liu, J., Wei, M., Shi, R., Elsworth, D., 2018. Why shale permeability changes under variable effective stresses: new insights. Fuel 213, 55–71.

da Silva, M.R., Schroeder, C., Verbrugge, J.C., 2008. Unsaturated rock mechanics applied to a low-porosity shale. Eng. Geol. 97 (1–2), 42–52.

Dicker, A.I., Smits, R.M., 1988. A practical approach for determining permeability from laboratory pressure-pulse decay measurements. In: International Meeting on Petroleum Engineering. Society of Petroleum Engineers.

Economides, M., Nolte, K., 2000. Reservoir Stimulation, third ed. John Wiley and Sons.

Fan, M., Han, Y., McClure, J., Chen, C., 2017. Hydraulic fracture conductivity as a function of proppant concentration under various effective stresses: from partial monolayer to multilayer proppants. In: Unconventional Resources Technology Conference. https://doi.org/10.15530/URTEC-2017-2693347.

Fan, M., McClure, J., Han, Y., Li, Z., Chen, C., 2018. Interaction between proppant compaction and single-/multiphase flows in a hydraulic fracture. SPE-189985-PA. SPE J. https://doi.org/10.2118/189985-PA.

Gu, M., Mohanty, K.K., 2014. Effect of foam quality on effectiveness of hydraulic fracturing in shales. Int J Rock Mech Min 70, 273–285.

Gutierrez, M., Katsuki, D., Tutuncu, A., 2015. Determination of the continuous stress-dependent permeability, compressibility and poroelasticity of shale. Mar. Petrol. Geol. 68, 614–628.

Haskett, S.E., Narahara, G.M., Holditch, S.A., 1988. A method for simultaneous determination of permeability and porosity in low-permeability cores. SPE Form. Eval. 3 (3), 651–658.
Hayek, M., 2015. Exact solutions for one-dimensional transient gas flow in porous media with gravity and Klinkenberg effects. Transport Porous Media 107 (2), 403–417.
Hu, G., Wang, H., Fan, X., Yuan, Z., Hong, S., 2009. Mathematical model of coalbed gas flow with Klinkenberg effects in multi-physical fields and its analytic solution. Transport Porous Media 76 (3), 407.
Hu, T., Pang, X., Jiang, S., Wang, Q., Zheng, X., Ding, X., et al., 2018. Oil content evaluation of lacustrine organic-rich shale with strong heterogeneity: a case study of the Middle Permian Lucaogou Formation in Jimusaer Sag, Junggar Basin, NW China. Fuel 221, 196–205.
Hsieh, P.A., Tracy, J.V., Neuzil, C.E., Bredehoeft, J.D., Silliman, S.E., 1981. A transient laboratory method for determining the hydraulic properties of 'tight' rocks—I. Theory. In: International Journal of Rock Mechanics and Mining Sciences & Geomechanics Abstracts, vol. 18. Pergamon, pp. 245–252, 3.
Innocentini, M.D., Pandolfelli, V.C., 2001. Permeability of porous ceramics considering the Klinkenberg and inertial effects. J. Am. Ceram. Soc. 84 (5), 941–944.
Javadpour, F., 2009. Nanopores and apparent permeability of gas flow in mudrocks (shales and siltstone). J. Can. Petrol. Technol. 48, 16–21.
Jin, G., Pérez, H.G., Agrawal, G., Khodja, M.R., Ali, A.Z., Hussaini, S.R., Jangda, Z.Z., 2015. March). The impact of gas adsorption and composition on unconventional shale permeability measurement. In: SPE Middle East Oil & Gas Show and Conference. Society of Petroleum Engineers.
Jones, S.C., 1997. A technique for faster pulse-decay permeability measurements in tight rocks. SPE Form. Eval. 12 (1), 19–26.
Klinkenberg, L.J., 1941. The permeability of porous media to liquids and gases. In: Drilling and Production Practice. American Petroleum Institute.
Kwon, O., Kronenberg, A.K., Gangi, A.F., Johnson, B., 2001. Permeability of Wilcox shale and its effective pressure law. J. Geophys. Res.: Solid Earth 106 (B9), 19339–19353.
Li, C., Xu, P., Qiu, S., Zhou, Y., 2016. The gas effective permeability of porous media with Klinkenberg effect. J. Nat. Gas Sci. Eng. 34, 534–540.
Ojala, I.O., Fjær, E., 2007. The effective stress coefficient in porous sandstone. In: 1st Canada-US Rock Mechanics Symposium. American Rock Mechanics Association.
Rydzy, M.B., Patino, J., Elmetni, N., Appel, M., 2016. Stressed permeability in shales: effects of matrix compressibility and fractures—a step towards measuring matrix permeability in fractured shale samples. In: Paper ID: SCA2016-027, International Symposium of the Society of Core Analysts (SCA), Snowmass, CO.
Soeder, D.J., 1988. Porosity and permeability of eastern Devonian gas shale. SPE Form. Eval. 3 (2), 116–124.
Tian, Y., Yu, X., Li, J., Neeves, K.B., Yin, X., Wu, Y.S., 2019. Scaling law for slip flow of gases in nanoporous media from nanofluidics, rocks, and pore-scale simulations. Fuel 236, 1065–1077.
Vermylen, J.P., 2011. Geomechanical Studies of the Barnett Shale. Stanford University, Texas, USA.
Wang, G., Ren, T., Wang, K., Zhou, A., 2014. Improved apparent permeability models of gas flow in coal with Klinkenberg effect. Fuel 128, 53–61.
Warpinski, N.R., Teufel, L.W., 1992. Determination of the effective-stress law for permeability and deformation in low-permeability rocks. SPE Form. Eval. 7 (2), 123–131.
Wu, Y.S., Pruess, K., 1998. Gas flow in porous media with Klinkenberg effects. Transport Porous Media 32 (1), 117–137.
Zhu, W.C., Liu, J., Sheng, J.C., Elsworth, D., 2007. Analysis of coupled gas flow and deformation process with desorption and Klinkenberg effects in coal seams. Int. J. Rock Mech. Min. Sci. 44 (7), 971–980.